1992

B. Koren, H.T.M. van der Maarel

On steady, inviscid shock waves at continuously curved, convex surfaces

Department of Numerical Mathematics Report NM-R9202 February

CWI is the research institute of the Stichting Mathematisch Centrum, which was founded on February 11, 1946, as a non-profit institution aiming at the promotion of mathematics, computer science, and their applications. It is sponsored by the Dutch Government through the Netherlands organization for scientific research (NWO).

On Steady, Inviscid Shock Waves at Continuously Curved, Convex Surfaces

Barry Koren and Eric van der Maarel
CWI
P.O. Box 4079, 1009 AB Amsterdam, The Netherlands

Abstract

An accurate and efficient numerical method for the steady, 2-D Euler equations is applied to study steady shock waves perpendicular to smooth, convex surfaces. The main subject of study is the flow near both ends of the shock wave. Some doubts are formulated about the correctness of a known analytical model of the inviscid shock-foot flow. Yet, the numerical results presented do not show that this analytical model is incorrect. For the inviscid shock-tip flow, two existing analytical solutions are discussed. The numerical results presented agree with one of these. Good numerical accuracy is achieved through a solution-adaptive, higher-order accurate finite-volume discretization. Good computational efficiency is obtained by a multigrid acceleration technique.

1980 Mathematics Subject Classification: 65Bxx,65N50,76H05,76L05.
Key Words and Phrases: shock waves, grid refinement, multigrid acceleration.
Note: This work was performed as part of a BRITE/EURAM Area 5 project, under Contract No. AERO-0003/1094.

1. Introduction

Near shock waves appearing with local supersonic zones in steady, inviscid flows along continuously curved, convex walls (Figure 1), the following two intriguing flow regions exist:

- the flow region where the shock wave abuts the continuously curved, convex wall (the shock-foot region) and
- the flow region near the other end of the shock wave (the shock-tip region).

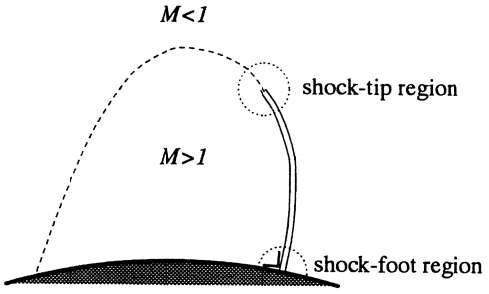

Figure 1. Shock wave fencing off local supersonic zone along continuously curved, convex wall.

Report NM-R9202
ISSN 0169-0388
CWI
P.O. Box 4079, 1009 AB Amsterdam, The Netherlands

In this section we start by reviewing some known studies of the local flow in both regions. Herewith we particularly look at aspects like accuracy and - in case of numerical studies - also efficiency. In the following, the shock foot and shock tip are defined as the lower and upper end point (not segment) of the shock wave.

1.1. Shock-foot region

1.1.1. Normal shock with normal extension. Concerning the shock-foot flow, the following physically interesting situation occurs. By imposing the condition that the flow does not change direction when passing through the shock foot, the shock is necessarily normal to the surface and hence, passing through the shock foot, the gas motion satisfies the normal-shock relations. Considering a shock wave which remains normal to some (arbitrary) distance above the surface (Figure 2), the normal-shock relations remain valid up to this distance. In the following we refer to such a shock as a normal shock with normal extension.

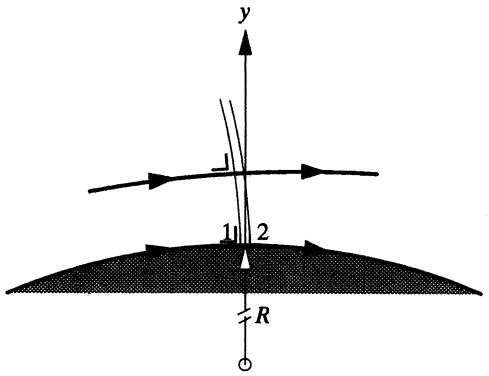

Figure 2. Normal shock with normal extension.

Along the continuously curved surface sketched in Figure 2, the gas motion also satisfies the equation of curvilinear motion

$$\frac{\partial p}{\partial y} = \frac{\gamma p M^2}{R}, \tag{1}$$

with y the coordinate normal to the wall and R the radius of curvature of the wall. (Throughout this paper, R is assumed to be finite.)

It may be apparent that for a normal shock with normal extension, the post-shock flow which has just satisfied the normal-shock relations, does not necessarily satisfy equation (1) any longer. We show that this is indeed the case by deriving that for a normal shock wave with normal extension, only one specific Mach number at the upstream shock-foot face exists, for which passage through the normal shock foot does not lead to a conflict with respect to satisfaction of the equation of curvilinear motion at the downstream shock-foot face. For this we introduce the subscripts 1 and 2 for the up- and downstream shock-foot face, respectively (Figure 2). Applying equation (1) at the downstream shock-foot face, we have

$$\frac{\partial p_2}{\partial y} = \frac{\gamma p_2 M_2^2}{R}. \tag{2a}$$

Alternatively, we also write for $\frac{\partial p_2}{\partial y}$:

$$\frac{\partial p_2}{\partial y} = \frac{\partial}{\partial y}\left(\frac{p_2}{p_1}\right) p_1 + \frac{p_2}{p_1}\frac{\partial p_1}{\partial y}. \tag{2b}$$

We proceed by expressing $\frac{\partial p_2}{\partial y}$ according to (2a) and (2b) in terms of the pre-shock flow. For the post-shock terms p_2 and M_2^2 occurring in equations (2a)-(2b), we can directly write:

$$p_2 = \frac{2\gamma M_1^2 - (\gamma - 1)}{\gamma + 1} p_1, \tag{3a}$$

$$M_2^2 = \frac{2 + (\gamma - 1)M_1^2}{2\gamma M_1^2 - (\gamma - 1)}. \tag{3b}$$

Further, for the pressure gradient $\frac{\partial p_1}{\partial y}$ in (2b), we have

$$\frac{\partial p_1}{\partial y} = \frac{\gamma p_1 M_1^2}{R}. \tag{3c}$$

The gradient term $\frac{\partial}{\partial y}\left(\frac{p_2}{p_1}\right)$ in (2b) requires some work. Given the normal extension of the shock wave, we may use the normal shock relation (3a) for rewriting this gradient term. It follows that $\frac{\partial}{\partial y}\left(\frac{p_2}{p_1}\right) = \frac{4\gamma}{\gamma+1} M_1 \frac{\partial M_1}{\partial y}$, which - assuming the pre-shock flow to be isentropic and applying (3c) - leads to

$$\frac{\partial}{\partial y}\left(\frac{p_2}{p_1}\right) = \frac{-4\gamma}{\gamma + 1}\left(1 + \frac{\gamma - 1}{2} M_1^2\right)\frac{M_1^2}{R}. \tag{3d}$$

Equating (2a)-(2b) and substituting (3a)-(3d), yields then the following compact quadratic equation for M_1^2:

$$M_1{}^4 - (\gamma + 1)M_1^2 - 1 = 0. \tag{4}$$

From equation (4) it follows that the only specific Mach number M_1 - to be further denoted by $M_1^\star$ - which allows a normal shock wave with normal extension, is:

$$M_1^\star = \sqrt{\frac{\gamma + 1}{2} + \sqrt{\left(\frac{\gamma + 1}{2}\right)^2 + 1}}. \tag{5}$$

In more cumbersome derivations, this specific Mach number was already found by Tsien (1947), Lin and Rubinov (1948), and Zierep (1958a).

1.1.2. Normal shock with oblique extension. Concerning the flow in the shock-foot region for Mach numbers M_1 different from $M_1^\star$, Zierep (1958a) has obtained further analytical results. In this section we review some of these results.

Zierep (1958a) found the known result that at the downstream side of the shock foot, for $M_1 \neq M_1^\star$ - in general - a singular solution must occur, which has the following property: in its foot, the shock wave has an infinitely large curvature. In analogy to the normal shock with normal extension as depicted in Figure 2, the present shock can be illustrated as has been done in Figure 3. At an arbitrarily small distance above the surface it already has a finite degree of obliquity. This singular change from normal shock wave (in the foot) to oblique shock wave (immediately above the foot) implies that at the downstream shock-foot face an infinitely steep decrease in the surface pressure occurs, which ensures that the conflict with respect to satisfaction of the equation of curvilinear motion at the downstream shock-foot face, which was mentioned in the previous section, does not occur. In the following we refer to shocks of this type as normal shocks with oblique extension.

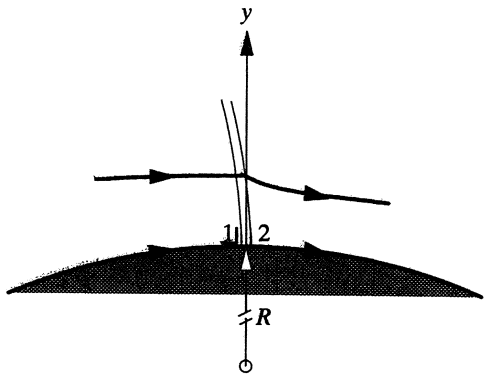

Figure 3. Normal shock with oblique extension.

Support for the correctness of this singular solution is seen to come from the fact that post-shock expansions (though not infinitely steep, see Figure 4) are really observed in the results of e.g. wind tunnel experiments. (For this support, Zierep (1958a) explicitly makes a reference to the classical experimental results of Ackeret *et al.* (1946).) In our opinion, the physics in these wind tunnel experiments is too different from inviscid physics to let them be of much support for the correctness of an inviscid analysis.

Instead of from e.g. wind tunnel experiments, in our opinion, support for at least the singular behavior of the post-shock surface pressure simply comes from theory. Viz., if the post-shock pressure correction would have a finite steepness (Figure 4b), there would probably be a finite region in which the equation of curvilinear motion is not satisfied, which - in a steady flow - is physically impossible.

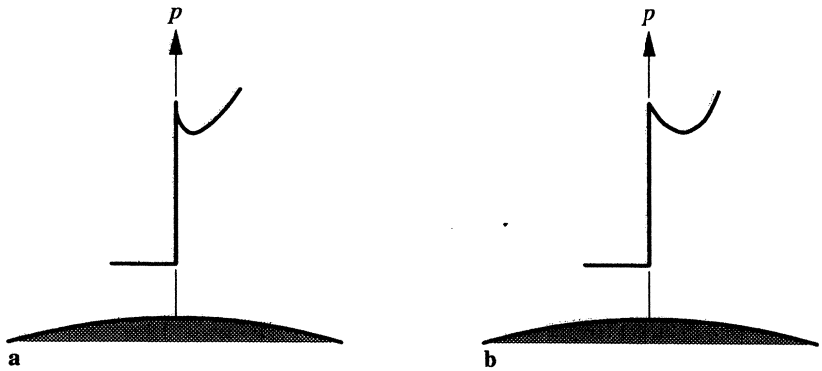

Figure 4. Post-shock surface pressure corrections:
(a) infinitely steep expansion, (b) finitely steep expansion.

However, concerning the correctness of the specific singular solution found by Zierep, from a theoretical point of view, also doubts arise. First, although Zierep's analysis starts with the full Euler equations, in becoming local (i.e. in approaching the wall along the shock wave), to these starting equations it applies some simplifications which are based on questionable pre-assumptions about how the flow locally behaves there. Second, we have the following more specific doubts about the correctness of this singular solution. According to it, the normal shock with oblique extension cannot exist in the range $(M_1^{\star}, M_1^{\star\star}]$, with $M_1^{\star}$ satisfying relation (5) and with $M_1^{\star\star}$ satisfying

$$M_1^{\star\star} = \sqrt{\frac{2 + \frac{\gamma+1}{2}}{2 - \frac{\gamma+1}{2}}}. \tag{6}$$

(Notice that for any admissible value of γ - i.e. any γ from the range [1,3] - it holds $M_1^{\star} < M_1^{\star\star}$.)

Though we do not know any example of a steady shock wave normal on a convex surface in the M_1-range $(M_1^{\star}, M_1^{\star\star}]$ indeed, a physical understanding of this remarkable range of non-existing shock waves is still missing. Further, concerning the upper bound $M_1^{\star\star}$ of this range, in the limit $M_1 \downarrow M_1^{\star\star}$ Zierep's solution becomes so much singular that it conflicts with the standard, uncurved-shock relations that were used in deriving it. To give some evidence of this discrepancy, we consider the bi-segmental piece of shock wave which is depicted in Figure 5. This stylized piece of shock wave is to be regarded as a discretization of the exact shock wave, which latter has been indicated with dotted lines in Figure 5. The bi-segmental piece of shock wave consists of a segment which stands normal on the wall and of an oblique segment on top of that. The foot of the normal segment and the tip of the oblique segment are tangent to the exact shock wave. The segments have the same length, so that the kink in the discrete shock wave is centered.

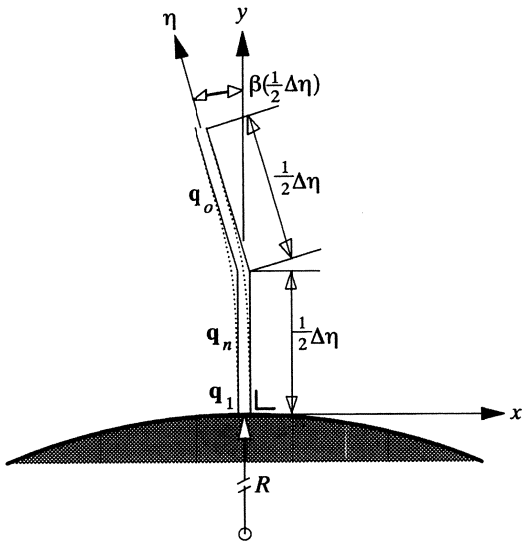

Figure 5. Bi-segmental piece of shock wave.

For this discrete, composite shock, we derive an expression for the transport of mass, x-momentum and y-momentum across its upstream face, per unit of length and time. (Concerning the transport of energy, the flow is assumed to be isenthalpic.) For this derivation, along the exact shock wave we introduce the coordinate η, that has the shock foot as origin. Next, we introduce the average gas states

$$\mathbf{q}_n \equiv \frac{\int_0^{\frac{1}{2}\Delta\eta} \mathbf{q}(\eta) d\eta}{\frac{1}{2}\Delta\eta} \quad \text{and} \tag{7a}$$

$$\mathbf{q}_o \equiv \frac{\int_{\frac{1}{2}\Delta\eta}^{\Delta\eta} \mathbf{q}(\eta) d\eta}{\frac{1}{2}\Delta\eta} \tag{7b}$$

at the upstream face of the normal and oblique segment, respectively (Figure 5). Then, for this transport vector per unit of length and time, to be further denoted by $\mathbf{F}$, we can write:

$$\mathbf{F} = \frac{1}{2}\mathbf{f}(\mathbf{q}_n) + \frac{1}{2}\cos\beta\,\mathbf{f}(\mathbf{q}_o) + \frac{1}{2}\sin\beta\,\mathbf{g}(\mathbf{q}_o), \tag{8}$$

in which

$$\mathbf{f}(\mathbf{q}) = \begin{pmatrix} \rho u \\ \rho u^2 + p \\ \rho u v \end{pmatrix} \quad \text{and} \tag{9a}$$

$$\mathbf{g}(\mathbf{q}) = \begin{pmatrix} \rho v \\ \rho v u \\ \rho v^2 + p \end{pmatrix}, \tag{9b}$$

with u and v the velocity components in x- and y-direction, respectively (Figure 5). In relation (8), the last two terms are due to the curvature of the shock wave. For the angle β in these two curvature terms we are going to use the detailed expression $\beta = \beta(\eta)$ given in Zierep (1958b) and we study the behavior of $\mathbf{F}$ in the limit $\Delta\eta \downarrow 0$. For $\beta = \beta(\eta)$, Zierep (1958b) gives

$$\beta(\eta) = \sqrt{2\sigma \frac{\eta}{R}}, \tag{10}$$

where, rewriting from Zierep (1958b),

$$\sigma = \sigma(M_1) = \frac{\lambda(M_1) - \frac{(\gamma+1)(M_1^2-1)\left(\gamma+\frac{\gamma^2+1}{\gamma+1}(M_1^2-1)\right)}{1-\gamma+(1+3\gamma)M_1^2}}{1 - 2\frac{(M_1^2-1)\left(\gamma+\frac{\gamma^2+1}{\gamma+1}(M_1^2-1)\right)}{\left(1-\gamma+(1+3\gamma)M_1^2\right)\left(1+\frac{\gamma-1}{\gamma+1}(M_1^2-1)\right)}}, \tag{11a}$$

with

$$\lambda(M_1) = \frac{(2+(\gamma-1)M_1^2)(1+\gamma M_1^2)}{1-\gamma+(1+3\gamma)M_1^2}, \tag{11b}$$

and with M_1 the Mach number at the upstream shock-foot face. As an example, in Figure 6 we depict $\sigma(M_1)$ for a di-atomic gas ($\gamma = \frac{7}{5}$), for which (5) and (6) yield: $M_1^\star \approx 1.662$, $M_1^{\star\star} = 2$.

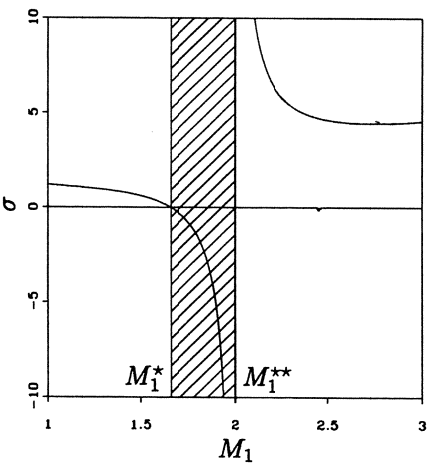

Figure 6. $\sigma = \sigma(M_1)$ from Zierep (1958b), for $\gamma = \frac{7}{5}$.

Given equation (11a), we verify:

- that a normal shock wave with normal extension as considered in section 1.1.1, can only occur for $M_1^\star$, because $\sigma(M_1) = 0$ for $M_1 = M_1^\star$ only,
- that no shock wave can occur in the M_1-range $(M_1^\star, M_1^{\star\star}]$ (the shaded range in Figure 6), because there it holds $\sigma(M_1) < 0$,
- that a very singular shock-foot flow occurs in the limit $M_1 \downarrow M_1^{\star\star}$, since $\lim_{M_1 \downarrow M_1^{\star\star}} \sigma(M_1) = \infty$, and

- that the shock wave has an infinitely large curvature in its foot for all (supersonic) $M_1 < M_1^{\star}$ and all $M_1 > M_1^{\star\star}$, because $\lim_{\eta \downarrow 0} \frac{d\beta}{d\eta} = \sqrt{\frac{\sigma(M_1)}{2\eta R}} = \infty$ for all these values of M_1.

Still a detail concerning the curvature of the shock wave in its foot at $M_1 = M_1^{\star}$: Zierep (1958a) finds that this curvature is zero. In our opinion, from the present theory this answer cannot be given, because in $\lim_{M_1 \uparrow M_1^{\star}} \lim_{\eta \downarrow 0} \frac{d\beta}{d\eta} = \sqrt{\frac{\sigma(M_1)}{2\eta R}} = \frac{0}{0}$, both limits can be taken strictly independent from each other (M_1 does not depend on η) and hence $\lim_{M_1 \uparrow M_1^{\star}} \lim_{\eta \downarrow 0} \frac{d\beta}{d\eta}$ is undetermined. For a finite (or even zero) shock curvature in the shock foot, $\sigma = 0$ is a necessary but insufficient condition.

With (10) and the Taylor-series expansion

$$\mathbf{q}(\eta) = \mathbf{q}_1 + \eta \frac{\partial \mathbf{q}_1}{\partial \eta} + \mathbf{O}(\eta^2), \tag{12}$$

where $\mathbf{q}_1$ is the gas state at the upstream shock-foot face (Figure 5), through successively (7a)-(7b) and (9a)-(9b), relation (8) for the flux vector $\mathbf{F}$ can be rewritten as

$$\begin{aligned}
\mathbf{F} = & \left[\mathbf{f}(\mathbf{q}_1) + \frac{1}{2}\Delta\eta \frac{\partial \mathbf{f}(\mathbf{q}_1)}{\partial \eta} + \mathbf{O}(\Delta\eta^2)\right] + \\
& \frac{1}{2}\left[\cos\left(\sqrt{\sigma \frac{\Delta\eta}{R}}\right) - 1\right]\left[\mathbf{f}(\mathbf{q}_1) + \frac{3}{4}\Delta\eta \frac{\partial \mathbf{f}(\mathbf{q}_1)}{\partial \eta} + \mathbf{O}(\Delta\eta^2)\right] + \\
& \frac{1}{2}\sin\left(\sqrt{\sigma \frac{\Delta\eta}{R}}\right)\left[\mathbf{g}(\mathbf{q}_1) + \frac{3}{4}\Delta\eta \frac{\partial \mathbf{g}(\mathbf{q}_1)}{\partial \eta} + \mathbf{O}(\Delta\eta^2)\right].
\end{aligned} \tag{13}$$

From expression (13) it appears that for finite values of σ, in the limit $\Delta\eta \downarrow 0$ - despite the infinite curvature - the standard, uncurved-shock relations can still be applied; the curvature terms vanish:

$$\begin{aligned}
\lim_{\Delta\eta \downarrow 0} \mathbf{F}_{\sigma<\infty} = & \lim_{\Delta\eta \downarrow 0}\left[\mathbf{f}(\mathbf{q}_1) + \frac{1}{2}\Delta\eta \frac{\partial \mathbf{f}(\mathbf{q}_1)}{\partial \eta} + \mathbf{O}(\Delta\eta^2)\right] + \\
& \lim_{\Delta\eta \downarrow 0}\left[-\frac{1}{4}\sigma \frac{\Delta\eta}{R} + \mathbf{O}(\Delta\eta^2)\right]\left[\mathbf{f}(\mathbf{q}_1) + \frac{3}{4}\Delta\eta \frac{\partial \mathbf{f}(\mathbf{q}_1)}{\partial \eta} + \mathbf{O}(\Delta\eta^2)\right] + \\
& \lim_{\Delta\eta \downarrow 0}\left[\sqrt{\sigma \frac{\Delta\eta}{R}} + \mathbf{O}(\Delta\eta^{\frac{3}{2}})\right]\left[\mathbf{g}(\mathbf{q}_1) + \frac{3}{4}\Delta\eta \frac{\partial \mathbf{g}(\mathbf{q}_1)}{\partial \eta} + \mathbf{O}(\Delta\eta^2)\right] = \mathbf{f}(\mathbf{q}_1).
\end{aligned} \tag{14}$$

However, from expression (13) it also appears that for infinitely large values of σ, in the limit $\Delta\eta \downarrow 0$, the influence of shock curvature cannot be neglected indeed. This shows the discrepancy in the Zierep model in the limit $M_1 \downarrow M_1^{\star\star}$.

1.1.3. Present shock-foot study. In the previous section we have made clear that some sound reasons exist which motivate a numerical study of steady Euler flow in the shock-foot region. In our numerical computations we apply the full, steady 2-D Euler equations in the complete computational domain. In doing so, we look at:

- the existence of a post-shock expansion as a function of M_1 and, if existing,
- its steepness for decreasing mesh width.

To get a good impression of the expansion's steepness for decreasing mesh width, without making excessive computational costs, we apply a technique which allows to efficiently zoom in at local flow features: a solution-adaptive multigrid technique. A description of this technique is given in section 2.

1.2. Shock-tip region

Concerning the shock-tip region, still today some uncertainties exist about how the shock wave merges into the main flow. Some authors claim that the shock wave becomes of vanishing strength into the direction of the sonic line (Figure 7a). Others claim that it bifurcates such that a triple-shock-configuration (or upside down λ-configuration) occurs (Figure 7b). Notice that a triple-shock-configuration must contain at least one additional discontinuity. In Courant and Friedrichs (1976, pp. 332-333), it is proved that three zones of different continuous states are impossible. (In Figure 7b we added a contact discontinuity.)

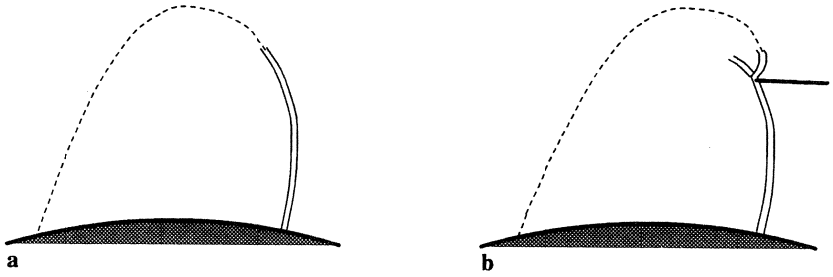

Figure 7. Two types of shock-tip configurations: (a) single-shock, (b) triple-shock.

Some profound analytical studies exist which support either the configuration in Figure 7a or that in Figure 7b. Representative examples of these studies are those of Germain and Gillon (1961), and Kraiko (1985), respectively. Germain and Gillon (1961) consider the transonic small perturbation equation and find through a hodograph method that the connection of the sonic line to the shock wave is in general tangent but distinguishable; generally the shock tip is a point of inflexion (i.e. at their connection, shock wave and sonic line have oppositely signed curvatures). According to Germain and Gillon, the entire shock wave is of strong type (so with transition from supersonic to subsonic speeds only). They conclude that other types of shock-tip configurations are possible, but only in exceptional cases. As opposed to this, Kraiko (1985) finds that the triple-shock-tip configuration sketched in Figure 7b is the commonly occurring one. Most present-day studies are in favor of this λ-configuration as being the most common one. A superficial physical reasoning supporting this is the known fact that in case of a convex surface, the compression waves (the waves propagating from the sonic line) are known to taper faster than the expansion waves (the waves running from the surface). The single-shock configuration in Figure 7a may be regarded as a special case of the triple-shock configuration, viz. with the shock-triple-point in the highest possible position.

Of all analytical studies on shock-tip configurations which are known to us, shortcomings are that they are local and use rather simplified equations, such as the transonic small perturbation equation. Though still with simplified equations, investigations of the local shock-tip flow as an integral part of a much more global flow have already been made numerically. Examples of such numerical studies are those of Murman (1974), Hafez and Cheng (1975), and Yu and Seebass (1976). Each of these three numerical works still considers the transonic small perturbation equation. Whereas the local tip flow certainly can be described by good approximation as a potential flow, the global flow generally cannot. Not only for studying the shock-foot flow, but also for studying the shock-tip flow, it makes sense to consider the full Euler equations. Further, in all numerical shock-tip work known to us, besides that no use is made of the Euler equations, also no use is made of locally refined grids. As a consequence, all of these numerical results are limited in accuracy by the use of both the simplified equations and the relatively coarse grids. (Concerning the latter,

Murman (1974) explicitly states that 'the exact structure at the shock tip cannot be resolved with the mesh considered'.) So, not only for the shock-foot flow, but also for the shock-tip flow, it makes sense to apply a grid refinement technique.

2. Solution-adaptive multigrid technique

2.1. Review

The following two types of solution-adaptive grid methods can be considered:

- grid movement methods and
- grid enrichment methods.

For a survey of both types of methods we refer to Berger (1987). The essential difference between both methods can be clarified by roughly stating that grid movement methods try to get a maximal accuracy for a fixed cost (a fixed number of grid points), whereas grid enrichment methods try to attain a fixed accuracy for a minimal cost (a minimal number of grid points). Difficulties of grid movement methods are:

- the simultaneous accurate resolution of more than one flow feature and
- the control over grid properties which are of importance to the specific discretization method considered (grid properties such as e.g. smoothness and orthogonality).

Difficulties of grid enrichment techniques are:

- to keep track (in the data structure) of the local refinements and
- to still assure conservation of mass, momentum and energy at the fine-coarse grid boundaries.

For the present flow features of interest (shock waves) we prefer to apply grid enrichment. Concerning grid enrichment, also two types of methods can be considered:

- nested methods and
- unnested methods.

Both methods apply fine subgrids overlying coarser grids. Whereas in the nested approach these fine grids are by definition aligned with the underlying coarser grids, in the unnested approach they are not necessarily so. An example of an unnested method in which (multi-dimensional) fluid flow equations are considered is the method of Fuchs (1990). Examples of nested methods considering (multi-dimensional) fluid flow equations, are the method of Berger and Jameson (1985) and the method of Van der Maarel (to appear). In our opinion, nested enrichment has a direct efficiency advantage over the unnested approach, because of its direct allowance for standard geometric multigrid acceleration. Besides the possibility to use it for acceleration, another interesting possibility of multigrid in this context is to apply it for estimating the local truncation error to be used for the refinement criterion. Further, the nested approach also has the advantage that satisfaction of conservation properties across aligned fine-coarse grid boundaries is more easily achieved than across non-aligned boundaries. For the present application we prefer nested enrichment; we proceed by further discussing it.

Without special care, in general, the set of nested, locally refined cells will be unstructured. Yet, structure can be obtained by properly clustering cells which are flagged to be refined. (For details on clustering we refer to Berger and Oliger (1984).) The previously mentioned method of Berger and Jameson (1985) is an example of a nested enrichment method which applies clustering. As opposed to that, the nested enrichment method of Van der Maarel (to appear) does not apply clustering. Concerning the mutual difference in efficiency between both nested approaches (the one without and the one with clustering), it is not clear to us which of both is most efficient. An obvious efficiency drawback of the approach without clustering is that one needs to keep track of all refined cells (as opposed to all refined subgrids only). Against that, clustering has of course the drawback of refining cells which are not actually flagged to be refined. Besides that, clustering may already by its use only, significantly increase the computational overhead. A major efficiency advantage of the clustered approach is then often said to come from its better possibilities for supercomputing. For vectorization, this is certainly true. For parallelization - in our opinion - the possibilities are the same.

Because of its successful application in another interesting flow problem (Van der Maarel and Koren, 1991), in the present paper we adhere to the nested enrichment technique without clustering. We proceed by briefly describing its data structure.

2.2. Data structure

A detailed description of the data structure of our nested enrichment method without clustering is given in Hemker *et al.* (1990). Here we just give a summary. We consider the steady, 2-D Euler equations on a domain $\Omega \subset \mathbb{R}^2$ with boundary $\partial\Omega$. In the discretization, Ω is approximated by a regular partition of disjoint quadrilateral cells. We consider grids on different levels of refinement, on each level employing a regular partition of one or more subdomains of Ω. The grid on level l is denoted by Ω_l, $l \in \{0, 1, 2, \ldots, \Lambda, \ldots, L\}$. The grids Ω_0 up to and including Ω_Λ completely cover Ω. Ω_0 is the coarsest grid and Ω_Λ is called the basic grid. Starting from $\Omega_{\Lambda+1}$ up to and including the finest grid Ω_L, the grids do not necessarily cover the complete domain Ω.

For $l > 0$, each cell of Ω_l is a member of a disjoint division (into a set of 2×2 smaller cells) of a cell of Ω_{l-1}. The cells of Ω_{l-1} and Ω_l are coexistent, i.e. coarse cells are not removed from the system when they are overlaid by fine cells. All cells in the geometric structure are related to each other through a so-called *quad-tree* data structure. The location of each cell of Ω_l is determined by a set of coordinates $(i, j) \in \mathbb{Z}^2$. A kid of cell $(\Omega_l)_{i,j}$ is either $(\Omega_{l+1})_{2i,2j}$, $(\Omega_{l+1})_{2i+1,2j}$, $(\Omega_{l+1})_{2i,2j+1}$ or $(\Omega_{l+1})_{2i+1,2j+1}$. The edge $(\partial\Omega_l)_{i,j}$ of $(\Omega_l)_{i,j}$ consists of four rectilinear sides. The grid Ω_l consists of a part Ω_l^f with cells that have been refined (i.e. have kids residing on level $l+1$), and a part Ω_l^c with cells that have not been refined (i.e. have no kids). The grids Ω_l^f and Ω_{l+1} cover the same part of Ω. The set of all non-refined cells is called the *composite* grid. It is the solution on the composite grid that we want to compute.

2.3. Discretization method and solution method

The present solution-adaptive multigrid method for the steady 2-D Euler equations is based on an existing non-adaptive multigrid method for the Euler equations. For details about this existing method, we refer to e.g. Hemker and Spekreijse (1986), and Koren (1988). Here we proceed by giving a brief summary only.

The method uses a cell-centered finite-volume discretization, in which an upwind numerical flux function (a shock capturing scheme) is applied. The solution method to be applied requires that the flux function is continuously differentiable. Well-known flux functions which satisfy this requirement are those of Van Leer (1982), and Osher and Solomon (1982). Because of its consistent

boundary-condition treatment and also for accuracy reasons, we prefer the scheme of Osher and Solomon. At each cell face this scheme approximately solves a 1-D Riemann problem. The discretization is first-order accurate by taking the left and right Riemann states equal to those in the corresponding adjacent finite volumes. Higher-order accuracy is obtained by applying higher-order accurate, piecewise polynomial state interpolation. To preserve monotonicity of the solutions, a limiter is used. The multigrid method which is applied for solving the system of discretized equations is nonlinear multigrid (NMG), with collective symmetric point Gauss-Seidel relaxation as the smoother. This method is very efficient for the first-order discretized Euler equations. Difficulties arising when applying it to higher-order discretized equations are circumvented by introducing iterative defect correction (IDeC) as an outer iteration to NMG.

In the present solution-adaptive multigrid method, the essentially new numerical ingredient is the computation of the left and right cell face states at the fine-coarse grid boundaries. In Van der Maarel (1992), a detailed description and accuracy analysis is given of the treatment of these inner boundaries. Here we briefly summarize the main features. Across a fine-coarse grid boundary, a difference of only one grid level is accepted. Along these boundaries, by proper interpolation from the local coarse-grid cell-center states, the locally missing fine-grid cell-center states are computed. These virtual states are then substituted into the numerical flux functions.

3. Numerical results

3.1. Test cases

Numerical computations are performed for flows of a di-atomic, perfect gas ($\gamma = \frac{7}{5}$) around a NACA0012-airfoil. The computations are started - in a non-adaptive way - on the uniform 8×5, O-type grid Ω_0 which is partially shown in Figure 8a. The far-field boundary is located at about 100 chord lengths from the airfoil. The computations are continued, through a nested iteration, up to and including $\Omega_\Lambda = \Omega_3$, the 64×40-grid which is partially depicted in Figure 8b. On top of Ω_3, local refinements are introduced. Details about the refinement schedule are discussed in section 3.2. In the nested iteration from Ω_0 up to and including $\Omega_\Lambda = \Omega_3$, the discrete equations solved are first-order accurate only. Starting from Ω_3 we begin to solve higher-order discretized equations; those corresponding to the limited $\kappa = 0$-scheme as introduced by Van Albada *et al.* (1982). (The motivation for applying the $\kappa = 0$-scheme is that this scheme gives the best convergence rate of iterative defect correction, as has been proved by Désidéri and Hemker (1990).

The following two far-field boundary-condition cases are considered:

- $M_\infty = 0.8$, $\alpha = 0$,
- $M_\infty = 0.8$, $\alpha = \alpha_{M_1^\star}$,

with M_∞ denoting the Mach number at the far-field inflow boundary and α the airfoil's angle of attack (incidence). The special incidence $\alpha_{M_1^\star}$ is that at which $M_1 = M_1^\star$. The first, symmetrical test case is arbitrarily chosen, so far as that we know from other computations that it yields a flow with shock wave for which $M_1 < M_1^\star$ (≈ 1.662 for $\gamma = \frac{7}{5}$). Hence, for the first test case we may expect a post-shock pressure correction. By local grid enrichment we study the corresponding shock-foot flow, as well as the corresponding shock-tip flow. The second test case, with $\alpha = \alpha_{M_1^\star}$, is studied to verify whether, in agreement with the analytical results from section 1.1.1, the numerical shock-foot flow is without any post-shock pressure correction indeed and - particularly - whether, in agreement with the solution of Zierep (1958a), it is at the limit of existence. Since

the value of $\alpha_{M_1^\star}$ is not known in advance, for the second test case we have to iterate on α. The α-iteration is described in the next section; it allows the capturing of a nice shock wave on the convex surface, somewhere in between nose and tail, and with M_1 converging to $M_1^\star$ in the limit of the iteration process. (The alternative approach of varying M_∞, while keeping $\alpha = 0$, cannot lead to $M_1 = M_1^\star$ for the NACA0012-airfoil.)

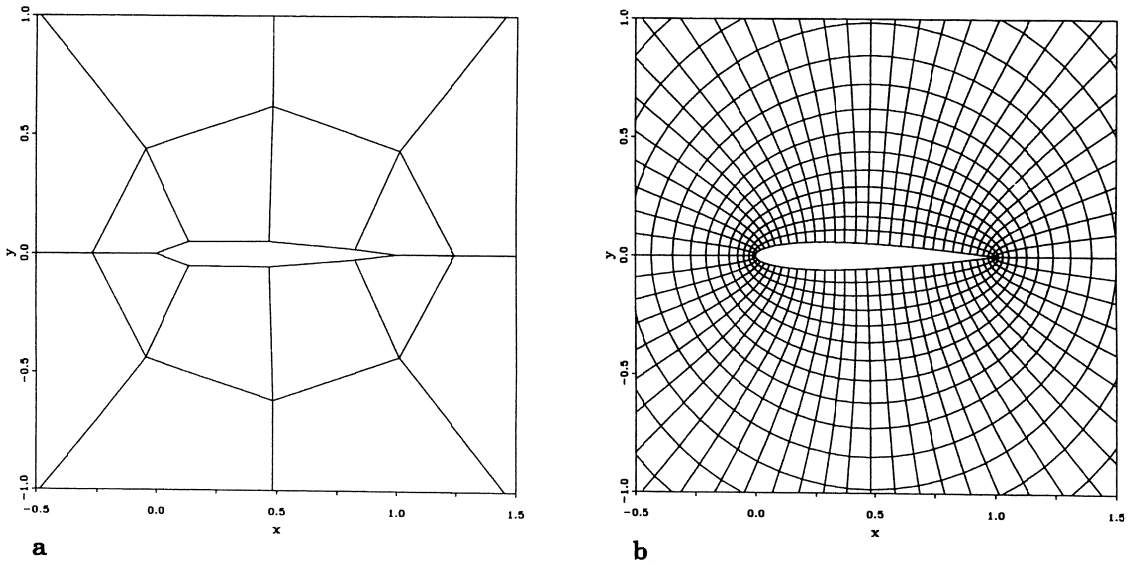

Figure 8. Details of coarsest grid and basic grid around NACA0012-airfoil: (a) 8×5-grid Ω_0, (b) 64×40-grid Ω_3.

3.2. Algorithm

In this section we give the solution-adaptive multigrid algorithm with incidence iteration. For this, we denote by $\tilde{N}_l(q_l) = 0$ and $N_l(q_l) = 0$ the first-order respectively second-order discretized Euler equations at grid level $l, l = 0, 1, \ldots, \Lambda, \ldots, L$. Further by $S_l(q_l)$ we denote the smoothing procedure, by I_{l-1}^l a prolongation operator, by NMG(l, q_l, r_l) the nonlinear multigrid algorithm (with r_l some right-hand side), and by $\| \cdot \|$ some suitable norm. Then, in quasi-Algol style the complete algorithm reads:

declarations:
integer l, Λ, L;
real $\alpha, \alpha_{\text{old}}, M_1, dM_1, (dM_1)_{\text{old}}, \gamma$, tolerances-of-NMG, -IDeC and -dM_1;
boolean incidence-correction, no-more-cells-added;
array q_l, r_l;

initializations:
incidence-correction := **true** (or **false**); $\alpha := 0$; q_0 := some initial solution; $q_0 := S_0(q_0)$;

nested iteration:
for $l := 1$ **step** 1 **until** Λ **do** $q_l := I_{l-1}^l q_{l-1}$; NMG$(l, q_l, 0)$;

nonlinear multigrid iteration:
until $\| \tilde{N}_\Lambda(q_\Lambda) \| <$ tolerance-of-NMG **do** NMG$(\Lambda, q_\Lambda, 0)$;
NMG$(\Lambda, q_\Lambda, 0)$;

defect correction iteration:
until $\| N_\Lambda(q_\Lambda) \| <$ tolerance-of-IDeC **do** NMG$(\Lambda, q_\Lambda, \tilde{N}_\Lambda(q_\Lambda) - N_\Lambda(q_\Lambda))$;

incidence iteration:
if incidence-correction **then**
begin
$dM_1 := (M_1)_\Lambda - M_1^\star$; $\alpha_{\text{old}} := \alpha$; $\alpha := 1°$;
until $\| N_\Lambda(q_\Lambda) \| <$ tolerance-of-IDeC **do** NMG$(\Lambda, q_\Lambda, \tilde{N}_\Lambda(q_\Lambda) - N_\Lambda(q_\Lambda))$;
$(dM_1)_{\text{old}} := dM_1$; $dM_1 := (M_1)_\Lambda - M_1^\star$;
until $dM_1 <$ tolerance-of-dM_1 **do**
begin
$\alpha := \alpha - \frac{dM_1}{\frac{dM_1 - (dM_1)_{\text{old}}}{\alpha - \alpha_{\text{old}}}}$; $\alpha_{\text{old}} := \alpha$;
until $\| N_\Lambda(q_\Lambda) \| <$ tolerance-of-IDeC **do** NMG$(\Lambda, q_\Lambda, \tilde{N}_\Lambda(q_\Lambda) - N_\Lambda(q_\Lambda))$;
$(dM_1)_{\text{old}} := dM_1$; $dM_1 := (M_1)_\Lambda - M_1^\star$;
end;
end;

grid adaptation:
for $l := \Lambda + 1$ **step** 1 **until** L **do**
begin
no-more-cells-added := **false**;
until no-more-cells-added **do**
begin
adapt $\{\Omega_\Lambda, \ldots, \Omega_l\}$;
until $\| N_l(q_l) \| <$ tolerance-of-IDeC **do** NMG$(l, q_l, \tilde{N}_l(q_l) - N_l(q_l))$;
end;
if incidence-correction **then**
begin
$dM_1 := (M_1)_l - M_1^\star$;
until $dM_1 <$ tolerance-of-dM_1 **do**
begin
$\alpha := \alpha - \frac{dM_1}{\frac{dM_1 - (dM_1)_{\text{old}}}{\alpha - \alpha_{\text{old}}}}$; $\alpha_{\text{old}} := \alpha$;
no-more-cells-added := **false**;
until no-more-cells-added **do**
begin
adapt $\{\Omega_\Lambda, \ldots, \Omega_l\}$;
until $\| N_l(q_l) \| <$ tolerance-of-IDeC **do** NMG$(l, q_l, \tilde{N}_l(q_l) - N_l(q_l))$;
end;
$(dM_1)_{\text{old}} := dM_1$; $dM_1 := (M_1)_l - M_1^\star$;
end;
end;
end

For a similar, quasi-Algol description of the nonlinear multigrid algorithm NMG(l, q_l, r_l) we refer to Hackbusch (1985). Notice that the incidence iteration is a Newton iteration which is free in the sense that it allows values of α for which $(M_1)_l$ lies in the 'forbidden' range $(M_1^\star, M_1^{\star\star}]$. (We allow this wittingly in order to investigate the existence of this range.) Notice further that the defect correction iteration applies one nonlinear multigrid cycle per IDeC-cycle only. (In Koren (1988),

this IDeC-cycling was found to be the most efficient.) Concerning the grid-adaptation procedure adapt $\{\Omega_\Lambda, \ldots, \Omega_l\}$, we simply check for each finite volume on the composite grid whether, for any of its four cell faces, a sonic point occurs along one of the four corresponding wave paths in state space. If one (or more) sonic points are detected, that cell, as well as some buffer zone of neighboring cells on the composite grid, are flagged to be refined. An important detail in this wave path approach is that it is not considered in cell face normal direction nor in a possible shock wave direction, but - instead - in flow direction. In computing the flow direction at each cell face, use is made of the density-dependent relation derived in Koren and Hemker (to appear). An objection that can be made against this sonic-point-wise enrichment is that although the accuracy of the numerical solution is improved, the degree of improvement may be small, because cells with large errors may remain coarse and hence persistent in keeping the global solution accuracy low. However, concerning the alternative grid refinement approach which equidistributes the local truncation errors below some treshold value, we would like to remark that for the nonlinear Euler equations - in general - no rigorous guarantees are given about the level of the global discretization error for any finite level of truncation error. Though it is possible to also de-refine cells which have been refined once but no longer need to be so, here we do not do so. (In applying both refinements and de-refinements, in steady computations we have once observed periodically oscillating grids.)

With $\Lambda = 3$, with the tolerances for both $\| \tilde{N}_l(q_l) \|$ and $\| N_l(q_l) \|$ equal to 10^{-6}, and with the tolerance for dM_1 equal to 10^{-3}, the algorithm yields the results given in the next section.

3.3. Results

3.3.1. Results for $\alpha = 0$. For $\alpha = 0$ we considered $L = 5, 6, 7$ and we took the buffer zone of flagged cells equal to zero. In Figure 9, a detail of the various converged composite grids is given, with shown on these: the sonic lines.

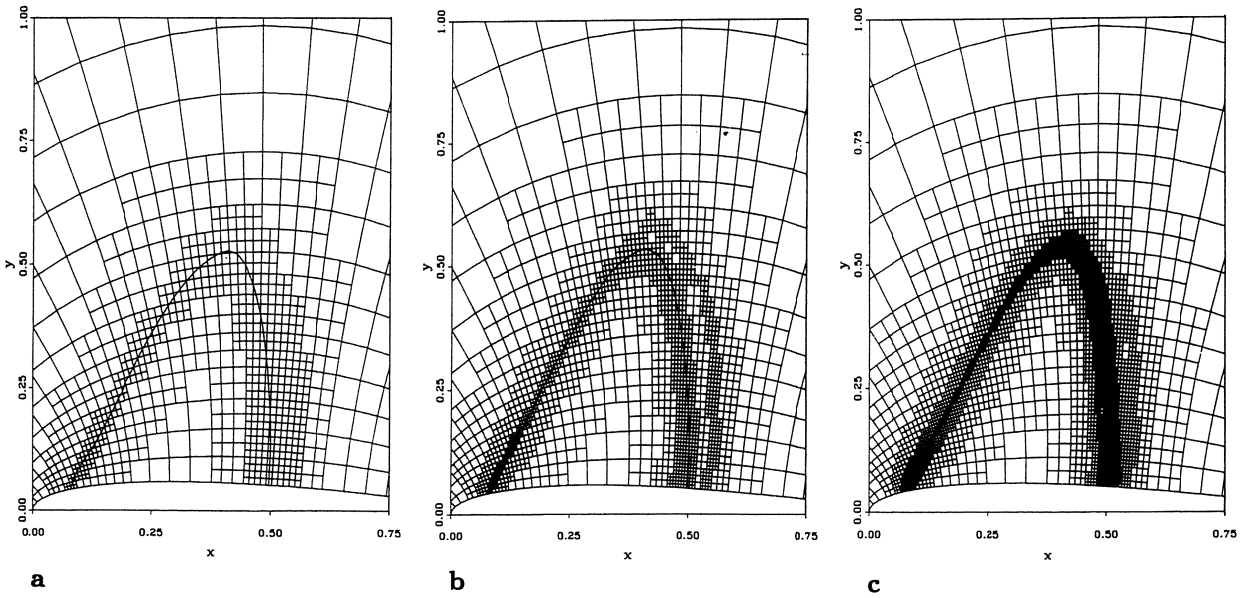

Figure 9. Converged composite grids with sonic lines, $\alpha = 0$:
(a) $L = 5$, (b) $L = 6$, (c) $L = 7$.

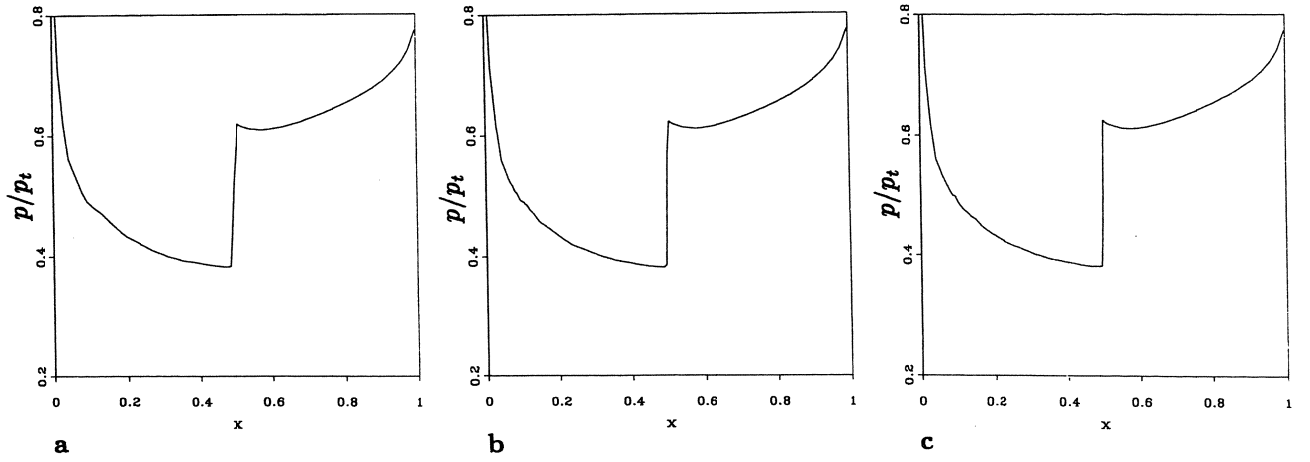

Figure 10. Surface pressure distributions, $\alpha = 0$:
(a) $L = 5$, (b) $L = 6$, (c) $L = 7$.

In Figure 10, the corresponding upper surface pressure distributions are given. Clearly visible in the latter figures is the occurrence of a post-shock expansion. We proceed by investigating the steepness of this expansion for decreasing mesh width. Assuming that in the exact solution, in conflict with theory, no infinitely steep post-shock expansion occurs ($\frac{\partial p_2}{\partial x} > -\infty$), we introduce the following expansion error δ_L:

$$\delta_L \equiv \left(\frac{\partial p_2}{\partial x}\right)_L - \frac{\partial p_2}{\partial x}, \tag{15a}$$

which we assume to be positive for all L. Then, given the assumed finity of the exact post-shock expansion and given the formal second-order of accuracy of the discretization method applied (see Van der Maarel (1992) for some formal evidence of this), we can certainly write

$$\delta_{L+1} = \left(\frac{1}{2}\right)^p \delta_L, \quad p > 0, \tag{15b}$$

where p denotes the local order of accuracy of the discretization method in the post-shock region. Given relations (15a)-(15b) and the previous assumptions, it should hold

$$\left(\frac{\partial p_2}{\partial x}\right)_{L-1} - \left(\frac{\partial p_2}{\partial x}\right)_L > \left(\frac{\partial p_2}{\partial x}\right)_L - \left(\frac{\partial p_2}{\partial x}\right)_{L+1}. \tag{15c}$$

In Table 1 we give the values of $\left(\frac{\partial p_2}{\partial x}\right)_L$ that we actually found in the numerical experiments for $L = 5, 6, 7$. It appears that relation (15c) is not satisfied by the present three numerical results, which - in agreement with theory - shows that the numerical post-shock expansion converges to an infinitely steep expansion.

Table 1. Post-shock expansions, $\alpha = 0$.

L	$\left(\frac{\partial p_2}{\partial x}\right)_L$
5	-0.28
6	-0.36
7	-0.50

Concerning the shock-tip flow, for all values of L considered, we did not observe the triple-shock-configuration as advocated by Kraiko (1985). The configurations found are like the one which is supported by Germain and Gillon; in all cases the shock does not bifurcate (see Figure 11 for one detailed view of this). The subtle inflexion point is not (yet) observed.

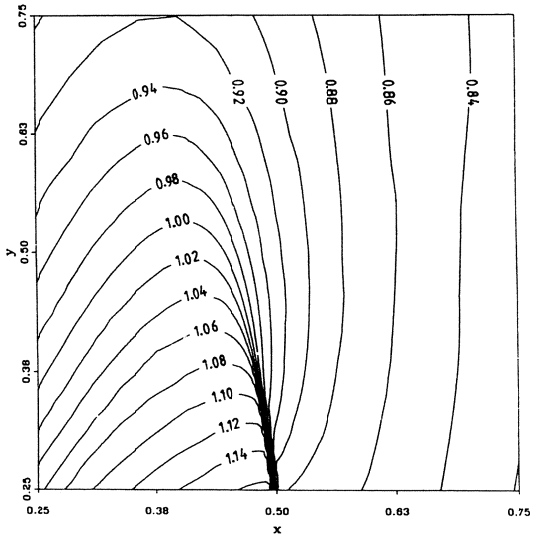

Figure 11. Mach number distribution around shock tip, $L = 7$, $\alpha = 0$.

3.3.2. Results for $\alpha = \alpha_{M_1^\star}$. For $\alpha = \alpha_{M_1^\star}$ we considered $L = 3, 4, 5$ and for the buffer zone - for reasons of robustness - we took two cells. Analogous to the previous results, in Figure 12 we give the converged composite grids with corresponding sonic lines and in Figure 13 the corresponding surface pressure distributions. The main thing that we notice from the surface pressure distributions is that the post-shock expansion has vanished indeed. In agreement with theory, downstream of the shock wave, all three surface pressure distributions in Figure 13 nicely show a pressure increase only. A remarkable phenomenon that we observed here for all three grid cases was non-convergence of the defect correction iteration NMG$(L, q_L, \tilde{N}_L(q_L) - N_L(q_L))$ (but still no divergence) as long as $(M_1)_L$ was in the range $(M_1^\star, M_1^{\star\star}]$ during the incidence iteration. The reason why we show here results for $L = 3, 4, 5$ only (instead of for $L = 5, 6, 7$ as we did for the previous test case) is that the solution method diverges for $L \geq 6$. Something related to this holds for the buffer zone of two cells to be refined additionally; with a buffer zone of less than two cells we diverged even for $L = 5$. Concerning the shock-tip flow, similar to the results for $\alpha = 0$, the configurations found agree best with those of Germain and Gillon (1961).

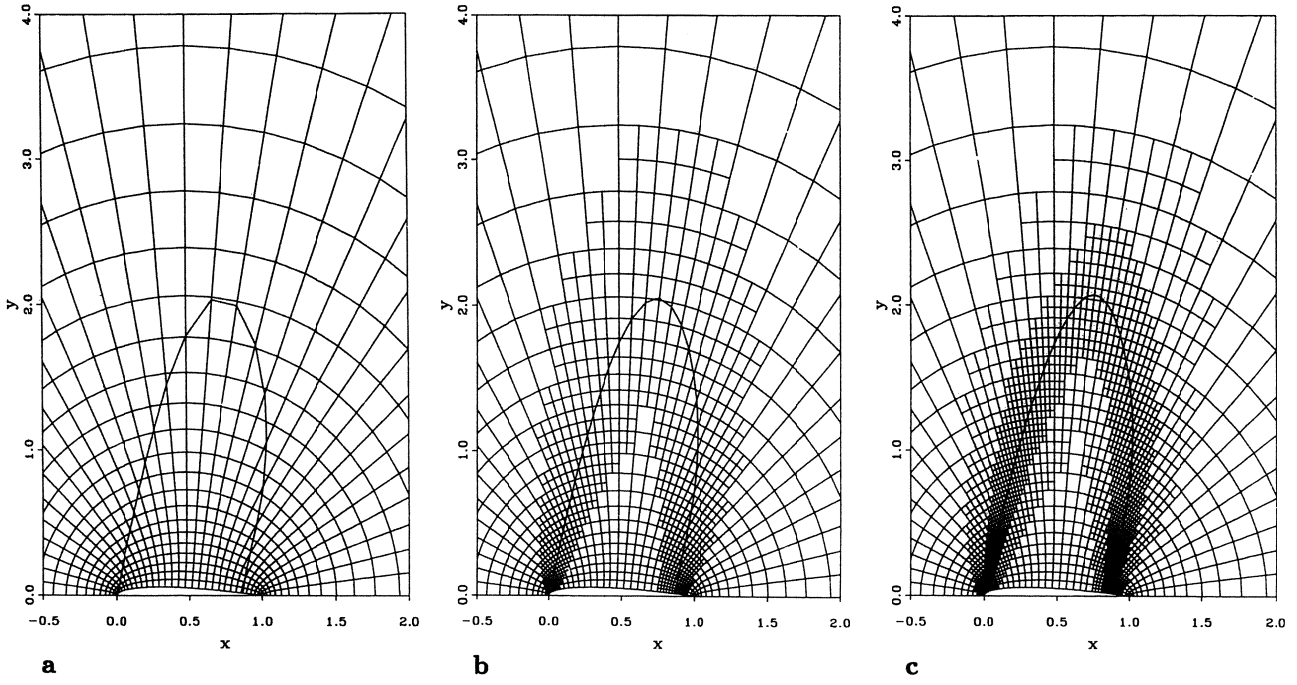

Figure 12. Converged composite grids with sonic lines, $\alpha = \alpha_{M_1^*}$: (a) $L = 3$, (b) $L = 4$, (c) $L = 5$.

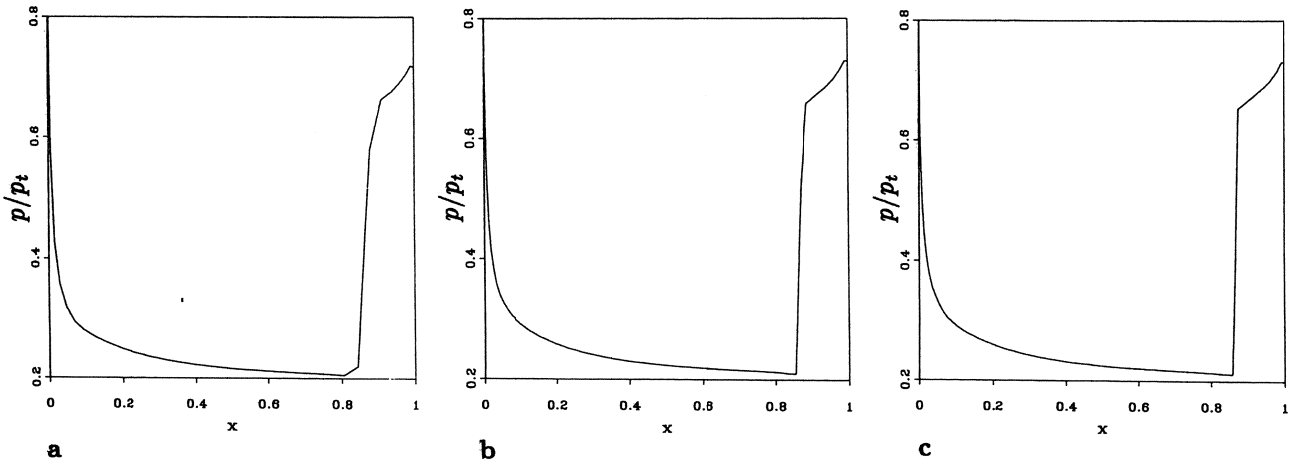

Figure 13. Surface pressure distributions, $\alpha = \alpha_{M_1^*}$: (a) $L = 3$, (b) $L = 4$, (c) $L = 5$.

The convergence problems that arose for this test case seem to indicate that indeed no steady shock wave perpendicular to the wall can exist in some range with $M_1^\star$ as the lower bound. A question which then arises is: if there is a steady flow solution beyond $M_1^\star$ which is still tangent to the wall, how does that flow solution look like ? A conjecture that we have with respect to this question is that for say increasing Mach number M_∞, a steady normal shock wave at $M_1^\star$ (a normal shock with normal extension) may bifurcate into two steady oblique shock waves (Figure 14a): a major oblique shock as the remainder of the single shock at $M_1^\star$ and - in front of that - a minor oblique shock, which has just developed. (Both shocks have a common shock foot and stand oblique on the wall in such a way that the flow remains tangent to the wall when passing through the double-shock foot.) Starting from a configuration as depicted in Figure 14a, for decreasing Mach number M_∞, the acute angle between both oblique shock waves in their common foot is supposed to converge to zero; the double-shock-foot configuration is supposed to transform into a normal, single-shock-foot configuration at $M_1^\star$. As opposed to that, for increasing Mach number M_∞, the minor shock is supposed to further increase in strength, size and obliquity. A nice feature of the double-shock-foot configuration in Figure 14a is its possible relation with the triple-shock-tip configuration from Figure 7b. Whereas the single-shock-tip configuration from Figure 7a could be considered as a special case of this triple-shock-tip configuration, viz. with the shock-triple-point in the highest possible position, the double-shock-foot configuration from Figure 14a may be considered as the other extreme case of the shock-triple-point configuration, viz. with the shock-triple-point in the lowest possible position. From this viewpoint, it might be possible to match analytical solutions for the flow in the shock-tip region on the one side and the flow in the shock-foot region on the other side.

Possibly a steady double-shock-foot configuration as depicted in Figure 14a can only exist for very specific boundary conditions. Solutions that will certainly prevail over this double-shock-foot solution are those which simply have an oblique single-shock foot (Figure 14b). In these flow solutions the flow is separated from the wall in passing through the shock foot and no unique (inviscid) solution exists in the separation zone. These solutions are probably mostly unsteady.

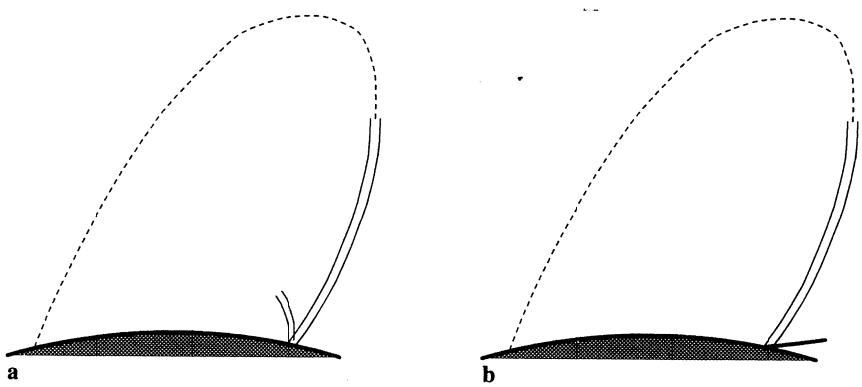

Figure 14. Possible oblique shock-foot configurations beyond normal, single-shock-foot configuration at $M_1^\star$:
(a) double-shock foot (without separation),
(b) single-shock foot (with separation).

Concerning this supposed unsteadyness, interesting results can be found in Dervieux *et al.* (1989), where for a circular cylinder at $M_\infty = 0.5$, Euler flow results are presented which have been obtained by various numerical methods. It is interesting to see that when using unsteady numerical methods for this circular-cylinder test-case, fully subsonic initial solutions first seem

to evolve to a specific quasi-steady solution, which becomes unsteady when continuing the time integration. Inspecting all circular-cylinder results in Dervieux *et al.* (1989), our conjecture is that the aforementioned, specific quasi-steady solution is at $M_1 = M_1^\star$. It seems that the genesis of unsteadyness is when M_1 exactly equals $M_1^\star$. Results which make this particularly plausible are those of Pandolfi and Larocca (1989), and Satofuka and Morinishi (1989).

4. Conclusions

Despite the theoretical doubts expressed about the correctness of Zierep's solution for the shock-foot flow, from the numerical results also presented in this paper no evidence has arisen which says that Zierep's solution is wrong in the practically relevant M_1-range $(1, M_1^\star)$. In fact we only disagree with Zierep about the detail that at $M_1 = M_1^\star$ the shock wave is uncurved in its foot; in our opinion this curvature is (still) undetermined. Concerning the singular shock curvature as found by Zierep for $M_1 < M_1^\star$ and $M_1 \geq M_1^{\star\star}$, we have investigated whether there is a discrepancy between, on the one hand, the result that in its foot the shock has an infinite curvature and, on the other hand, the uncurved-shock relations that Zierep applied in deriving this result. We have found that in fact only for $\lim M_1 \downarrow M_1^{\star\star}$ there is such a discrepancy. However, it is very likely that with increasing Mach number, at $M_1 = M_1^\star$ the normal single-shock-foot configuration changes into a qualitatively different shock-foot configuration which, for further increasing Mach numbers, never rechanges into the original normal single-shock-foot configuration.

Our main suggestion for further research is to make a qualitative study of the different possible shock-foot-flow solutions beyond $M_1 = M_1^\star$. Given the possible change at $M_1 = M_1^\star$ from steadyness to unsteadyness, such a study might be of some practical relevance as well (buffeting). It would be interesting to also invoke the shock-tip configuration in such an analysis.

Concerning the present solution-adaptive multigrid method, this seems to be an accurate and efficient tool for detailed studies of various other phenomena from steady gas dynamics.

References

Ackeret, J., Feldmann, F., and Rott, N. (1946). Untersuchungen an Verdichtungsstössen und Grenzschichten in schnell bewegten Gasen. *Mitteilungen aus dem Institut für Aerodynamik 10.*

Berger, M.J. (1987). Adaptive finite difference methods in fluid dynamics. *VKI Lecture Series 1987-04.*

Berger, M.J., and Jameson, A. (1985). Automatic adaptive grid refinement for the Euler equations. *AIAA J.*, **23**, 561-568.

Berger, M.J., and Oliger, J. (1985). Adaptive mesh refinement for hyperbolic partial differential equations. *J. Comput. Phys.*, **53**, 484-512.

Courant, R., and Friedrichs, K.O. (1976). *Supersonic Flow and Shock Waves.* Springer, New York.

Dervieux, A., Van Leer, B., Périaux, J., and Rizzi, A., eds. (1989). *Numerical Simulation of Compressible Euler Flows.* Vieweg, Braunschweig.

Désidéri, J.-A., and Hemker, P.W. (1990). Analysis of the convergence of iterative implicit and

defect-correction algorithms for hyperbolic problems. *CWI Report NM-R9004.*

Fuchs, L. (1990). Calculation of flow fields using overlapping grids. In *Proceedings of the Eighth GAMM-Conference on Numerical Methods in Fluid Mechanics* (P. Wesseling, ed.), pp. 138-147. Vieweg, Braunschweig.

Germain, P., and Gillon, G. (1961). Ecoulements transsoniques au voisinage d'un point de rencontre d'une onde de choc et d'une ligne sonique. *ONERA Publication 102.*

Hackbusch, W. (1985). *Multi-Grid Methods and Applications.* Springer, Berlin.

Hafez, M.M., and Cheng, H.K. (1975). Convergence acceleration and shock fitting for transonic aerodynamics computations. *AIAA Paper 75-51.*

Hemker, P.W., and Spekreijse, S.P. (1986). Multiple grid and Osher's scheme for the efficient solution of the steady Euler equations. *Appl. Numer. Math.*, **2**, 475-493.

Hemker, P.W., Van der Maarel, H.T.M., and Everaars, C.T.H. (1990). BASIS: A data structure for adaptive multigrid computations. *CWI Report NM-R9014.*

Koren, B. (1988). Defect correction and multigrid for an efficient and accurate computation of airfoil flows. *J. Comput. Phys.*, **77**, 183-206.

Koren, B., and Hemker, P.W. (to appear). Multi-D upwinding and multigridding for steady Euler flow computations. In *Proceedings of the Ninth GAMM-Conference on Numerical Methods in Fluid Mechanics.* (A. Rizzi and I.L. Ryhming, eds.). Vieweg, Braunschweig.

Kraiko, A.N. (1985). On the configuration of shock waves enclosing a local supersonic zone. *P.M.M. USSR*, **49**, 179-183.

Lin, C.C., and Rubinov, S.I. (1948). On the flow behind curved shocks. *J. Math. Phys.*, **27**, 105-129.

Murman, E.M. (1974). Analysis of embedded shock waves calculated by relaxation methods. *AIAA J.*, **12**, 626-633.

Osher, S., and Solomon, F. (1982). Upwind difference schemes for hyperbolic systems of conservation laws. *Math. Comput.*, **38**, 339-374.

Pandolfi, M. and Larocca, F. (1989). A contribution to the numerical prediction of transonic flows. In *Numerical Simulation of Compressible Euler Flows* (A. Dervieux, B. van Leer, J. Périaux and A. Rizzi, eds.), pp. 292-308. Vieweg, Braunschweig.

Satofuka, N., and Morinishi, K. (1989). Solution of compressible Euler flows using rational Runge-Kutta time stepping scheme. In *Numerical Simulation of Compressible Euler Flows* (A. Dervieux, B. van Leer, J. Périaux and A. Rizzi, eds.), pp. 309-330. Vieweg, Braunschweig.

Tsien, H.S. (1947). Flow conditions near the intersection of a shock wave with solid wall boundary. *J. Math. Phys.*, **26**, 69-75.

Van Albada, G.D., Van Leer, B., and Roberts, W.W. (1982). A comparative study of computational methods in cosmic gasdynamics. *Astron. Astrophys.*, **108**, 76-84.

Van der Maarel, H.T.M. (to appear). Adaptive multigrid for the Euler equations. *Comm. Appl. Numer. Meth.*.

Van der Maarel, H.T.M. (1992). Error estimation and refinement for 2-D, steady conservation laws, in multigrid context. *CWI Report NM-R92xx.*

Van der Maarel, H.T.M., and Koren, B. (1991). Spurious, zeroth-order entropy generation along a kinked wall. *Int. J. Numer. Meth. Fluids*, **13**, 1113-1129.

Van Leer, B. (1982). Flux-vector splitting for the Euler equations. In *Proceedings of the Eighth International Conference on Numerical Methods in Fluid Dynamics* (E. Krause, ed.), pp. 507-512. Springer, Berlin.

Yu, N.J., and Seebass, A.R. (1976). Inviscid transonic flow computations with shock fitting. In *Symposium Transsonicum II* (K. Oswatitsch and D. Rues, eds.), pp. 449-456. Springer, Berlin.

Zierep, J. (1958a). Der senkrechte Verdichtungsstoss am gekrümmten Profil. *ZAMP*, **IXb**, 764-776.

Zierep, J. (1958b). Der senkrechte Verdichtungsstoss am gekrümmten Profil. *DVL Bericht 51.*